ORIGINAL PAPER

Additively manufactured test phantoms for mimicking soft tissue radiation attenuation in CBCT using Polyjet technology

Sepideh Hatamikia [a,b,c,1,*], **Gunpreet Oberoi** [c,1], **Anna Zacher** [d], **Gernot Kronreif** [a], **Wolfgang Birkfellner** [c], **Joachim Kettenbach** [e], **Stefanie Ponti** [d], **Andrea Lorenz** [a], **Martin Buschmann** [f], **Laszlo Jaksa** [a], **Nikolaus Irnstorfer** [g], **Ewald Unger** [c]

[a] Austrian Center for Medical Innovation and Technology (ACMIT), Wiener Neustadt, Austria
[b] Research center for Medical Image Analysis and Artificial Intelligence (MIAAI), Department of Medicine, Faculty of Medicine and Dentistry, Danube Private University, Krems, Austria
[c] Center for Medical Physics and Biomedical Engineering, Medical University of Vienna, Vienna, Austria
[d] Preclinical Imaging Lab (PIL), Department of Biomedical Imaging and Image-guided Therapy, Medical University of Vienna, Vienna, Austria
[e] Institute of Diagnostic, Interventional Radiology and Nuclear Medicine, Landesklinikum Wiener Neustadt, Wiener Neustadt, Austria
[f] Department of Radiation Oncology, Medical University of Vienna, Vienna, Austria
[g] Division of Nuclear Medicine, Department of Biomedical Imaging and Image-guided Therapy at the Medical University of Vienna, Vienna, Austria

Received 6 January 2022; accepted 27 May 2022

Abstract

Objectives: To develop and validate a simple approach for building cost-effective imaging phantoms for Cone Beam Computed Tomography (CBCT) using a modified Polyjet additive manufacturing technology where a single material can mimic a range of human soft-tissue radiation attenuation.
Materials and Methods: Single material test phantoms using a cubic lattice were designed in 3-Matic 15.0 software . Keeping the individual cubic lattice volume constant, eight different percentage ratio (R) of air: material from 0% to 70% with a 10% increment were assigned to each sample. The phantoms were printed in three materials, namely Vero PureWhite, VeroClear and TangoPlus using Polyjet technology. The CT value analysis, non-contact profile measurement and microCT-based volumetric analysis was performed for all the samples.
Results: The printed test phantoms produced a grey value spectrum equivalent to the radiation attenuation of human soft tissues in the range of −757 to +286 HU on CT. The results from dimensional comparison analysis of the printed phantoms with the digital test phantoms using non-contact profile measurement showed a mean accuracy of 99.07 % and that of micro-CT volumetric analysis showed mean volumetric accuracy of 84.80–94.91%. The material and printing costs of developing 24 test phantoms was 83.00 Euro.
Conclusions: The study shows that additive manufacturing-guided macrostructure manipulation modifies successfully the radiographic visibility of a material in CBCT imaging with 1 mm^3 resolution, helping customization of imaging phantoms.

Keywords: CT; Cone Beam CT; Micro-CT; Additive manufacturing; Profilometer; Imaging phantoms; Material modification; Macrostructure; Radiation attenuation

* Corresponding author: Sepideh Hatamikia, Austrian Center for Medical Innovation and Technology (ACMIT), Wiener Neustadt, Austria.
[1] Joint First Author.

Z Med Phys **xxx** (2022) xxx–xxx
https://doi.org/10.1016/j.zemedi.2022.05.002
www.elsevier.com/locate/zemedi

1 Introduction

Cone-beam Computed Tomography (CBCT) is a moderately new imaging methodology that uses a cone-shaped X-ray beam to reconstruct a 3D image in a single rotation [1–4]. CBCT is more compact in size and affordable, exposes the patient to a lower radiation dose compared to conventional CT, and permits the patient to be in an upright position for assessment as well [1,5,6]. CBCT is widely used for analysis in oral and maxillofacial surgery as well as in vascular imaging and orthopedics [3,5,7–9].

Integration of CBCT panel to linear acceleration systems has made it also a significantly important tool for patient positioning and verification in image-guided radiation therapy (IGRT) particularly in intensity modulated radiation therapy (IMRT) [10]. It offers application in treatment planning, diagnosis and therapy and hence, it is interesting to advance its utility in healthcare [11]. Medical imaging has developed an interactive relationship with additive manufacturing (3D printing) giving the user opportunities for improved patient safety and therapy, training, education and research [12,13]. CBCT based additive manufacturing mainly finds application in image-guided treatment planning of maxillofacial disorders, quality assurance phantoms as well as radiotherapy tools such as brachytherapy molds, compensators, bolus, immobilizers and patient specific anthropomorphic phantoms [14,15].

Owing to the relative new CBCT modality, efforts are being made in combination with additive manufacturing to outline its Quality Assurance (QA) of image parameters like spatial resolution, image density values, image uniformity, noise, contrast detail and geometric accuracy [12,16,17]. With the availability of a wide range of 3D printing materials and technologies, existing phantoms have been built using Polyjet, Fused Deposition Modelling (FDM), stereolithography (SLA), Digital Light Processing (DLP) and casting with adequate tissue equivalency [18,19]. 3D printed imaging phantoms are relatively low-volume, accurate and cost-efficient with superior dimensional tolerance and ability to mimic complex-shapes [20]. Previous studies have shown the possibility to print tissue-equivalent radiodensity phantoms with FDM technology using a combination of 3D printing materials like acrylonitrile-butadiene-styrene (ABS), polylactic acid (PLA), polyethylene terephthalate (PETG), thermoplastic polyurethane (TPU), thermoplastic elastomer (TPE), polymers in different infill densities and by incorporating wooden or stonefil filaments to mimic radiation attenuation of a wide range of tissues [21–24]. However, these phantoms are limited by their uniformity in replication of radiation attenuation due to inhomogeneous distribution of multi-material, printing accuracy, and printing size restrictions of the FDM technology. There are also several studies in which the use of Polyjet technology to emulate tissue-like phantoms using different materials such as Agilus, VeroCyan, VeroClear, VeroBlackPlus, TangoPlus and TangoBlackPlus was proposed [25–27]. Polyjet technology is widely used due to its higher resolution (16–32 µm) and accuracy [18,28,29]. Each printing technology has pros and cons in the production of medical imaging models. FDM involves the process of layering molten thermoplastic polymers using a motor-driven head; it is beneficial for printing cost-efficient models, but the large nozzle size lowers the printing resolution at macrostructure level. In contrast, Polyjet involves the process of layering liquid photopolymers that are instantly cured with ultraviolet (UV) light. Polyjet enables simultaneous multi-material printing of a model with a large spectrum of distinct imaging parameters within a single print cycle with high resolution (32microns), but this technology can be impacted by support material removal especially in case of flexible macrostructures [29]. Additive manufacturing workflow gives the opportunity to design the macrostructure of a single material resulting in introduction of pores/ air gaps within the printed material. Consequently, the radiological and biomechanical properties of the material can be manipulated only by defining the percentage volume of air within the structure, without requisites of an additional material. In human skeleton, depending on the ratio of 'air: bone' within the tissues, the cortical and cancellous structures represent different densities on a radiograph. In our study, the rationale for material macrostructure manipulation to mimic the gradation in human soft tissue radiation attenuation is based on porous structure of bone tissue. In our knowledge, this bone-inspired biomimetic principle has not been applied before in the Polyjet printing technology, to create imaging phantoms built from a 'single' material. The modified single material possesses the capability to show a gradation of grey values mimicking human soft tissues in CBCT.

This study aims at enabling Polyjet technology to display a spectrum of radiodensity using a single material. The novelty of the research lies in designing a methodology in which one material can reproduce a variety of radiodensities of human soft tissues in CBCT with a resolution up to 1 mm^3 by altering the material macrostructure and hence can be used in printing customized patient-specific imaging phantoms including a wide range of radiodensities. TangoPlus FLX930 (TP), VeroClear RGD810 (VC) and Vero PureWhite RGD837 (VPW) were the photopolymers selected to 3D print the test structures for imaging phantoms as these are the most widely available materials used by Polyjet technology. A HU analysis from CT data was performed in order to evaluate the radiation attenuation property

Please cite this article as: Hatamikia, S., Oberoi, G., Zacher, A. et al., Additively manufactured test phantoms for mimicking soft tissue radiation attenuation in CBCT using Polyjet technology, Z Med Phys, https://doi.org/10.1016/j.zemedi.2022.05.002

of the printed phantoms. The reliability of the approach was validated by dimensional tolerance tests using micro-CT and non-contact measurement profilometer. The proposed method provides realistic patient-specific imaging phantoms for quality assurance and radiation therapy and opens the opportunities to imitate the complex heterogeneity within human tissues structures.

2 Materials and methods

In this study, additively manufactured imaging phantoms were designed and constructed. With this approach, a single material can mimic a range of grey values in CBCT by simply regulating the ratio of air: material. Three polymer materials commonly used with in-house Polyjet printer were used to print the test phantoms in 8 different air: material ratios for the study. The CBCT analysis and geometrical assessments were performed for all the samples.

2.1 Test phantom design

In this study, cylindrical test phantoms consisting of a 3D quadrilateral (cubic) lattice were developed by Polyjet additive manufacturing technology (Fig. 1 A). Considering the minimum layer thickness of the Polyjet printer (30 µm) and the post-printing processing, the length of the individual cubic lattice was selected to be 2.0 mm and was kept constant for each lattice design. Keeping the volume of the individual cubic lattice (V_c) constant, the lattice pillar volume (V_p) was changed to generate the desired R value (ratio of air: material) for the respective radiodensity in each of the three materials. To achieve an optimal visibility of the material lattice in CBCT, the ratios from 0% to 70% with a 10% increment were selected for the study. The following algorithm is proposed for reproducing tests phantoms with the desired grey value: if x is the length of each internal cubic lattice and s is the lattice pillar thickness, then the R value (ratio of air:material) is V_c/V_p can be subsequently calculated.

$$V_c = x^3$$

$$V_p = s^2(3x - 2s)$$

$$R = \frac{x^3}{s^2(3x - 2s)}$$

Eight digital cubic stereolithographic (STL) models were designed in 3-Matic 15.0 software (Materialize, Leuven, Belgium) for each R value (Fig. 1 B). For the printing process, 24 cylinders (8 for each material) with a height and diameter of 15.0 mm were derived from the corresponding STL files for the three different materials. The size of the STL files used for printing was between 1 to 2.8 Mb depending on the lattice structure.

2.2 Demonstration of an example use case for test phantoms

In order to further investigate the performance of the proposed method, we included additional experiments with a phantom consisting of different lattice structures and radiodensities. For this, a simplified anatomical model derived from an abdominal CT was used. An axial slice of this abdominal CT scan was segmented using 3D Slicer software 4.10.2 (Boston, MA, USA). Different organs and anatomical structures were identified and assigned to 6 different regions according to their dominating HU values. The segmented regions were exported as STL files, corrected to avoid holes and overlaps, downscaled to 45% of the size and provided with a thickness of 10 mm. The assignment of structures to the regions was done semi-automatically, using a region-growing approach in 3D Slicer (grow from seeds) with additional manual correction based on visual impression and to avoid too small regions.

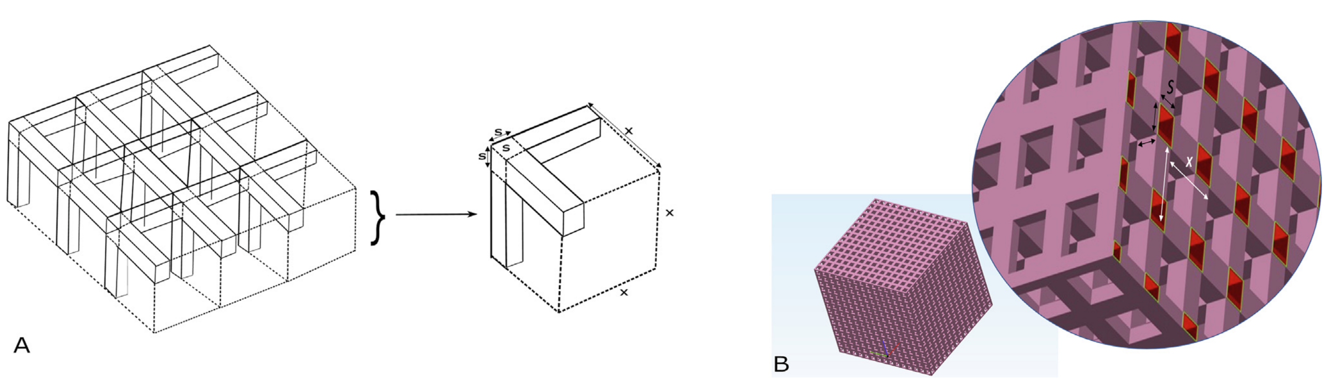

Figure 1. Test phantom design. A) The base design of the test phantom macrostructure. B) Stereolithographic (STL) file from the design process in Materialise 3-Matic software, x is the length of each internal cubic and s is the thickness of each pillar.

This model was used as a demonstration of a use case for the proposed cylindrical test phantom (Section 2.1) and includes more complex structures and combinations of different lattice structures within the same phantom. Based on the CT scan, the approximation of HU values within the abdomen CT were 759, 175, 96, 32, −65, −794 for bone, kidney/vessels, liver, connected tissue, surrounding body and lung, respectively. According to these approximate HU values in tissues, we then included lattice structures with the corresponding air: material ratios (R values) based on the prior density analysis of the cylindrical test phantoms (Section 2.1, 3.3 and 3.4). Fig. 2 represent the visualization of the STL file including different segmentations as well as designed lattice structures for the corresponding structures.

2.3 Material selection and multi-material printing

Vero PureWhite, VeroClear and TangoPlus polymers were selected to print the cylindrical test phantoms as well as an example used case phantom using on-site PolyJet^{TM} printer Connex3 Objet500 (Stratasys, EdenPrairie, MN, United States of America). For each structure of the use case phantom, a section with the related lattice structure was prepared and was used to build an intersection between lattice geometry and the tissue geometry. After assigning the R value based on individual tissue HU (Sections 3.3 and 3.4), the models were reassembled into their position according to the CT-scan to form the CT-phantom. 3-Matic 15.0 computer-aided designing (CAD) software was used to prepare the models. Based on the printing technology, it was imperative to separate the tissues as an individual shell to enable the PolyJet System to print the different parts with the defined material (VeroClear, TangoPlus, and Vero PureWhite) independent of their lattice structure. Based on the adjacent faces of the tissue shell they were glued together during the UV based print process. As post-processing steps, the models were then cleaned manually for gross support material (SUP706) removal and later flushed carefully using waterjet. The models were then placed in 2% sodium hydroxide solution for 24 hours and rinsed with water. We used a digital microscope VHX-7000 (Keyence, Keyence International, Mechelen, Belgium) to validate complete support material removal.

2.4 HU analysis using CT imaging and the two CBCT modalities used for scanning the test phantoms

The additively manufactured cylindrical test phantoms in three different materials with 8 different ratios (R1 to R8) of air:material as well as example use case phantom were scanned using the CT (SOMATOM Definition AS, Siemens Healthineers, Erlangen, Germany) with 120 kV, 61 mAs and 1 mm^3 voxel size in order to evaluate their radiodensities. To calculate radiodensity of cylindrical phantoms, 3D Slicer software was used to crop the CT volume at different ROIs (regions of interest) from individual cube of all the three materials (R1-R8). Then, Matlab software was used to calculate the average and standard deviation over the HU values for each cropped ROI and the HU values related to R1-R8. To calculate radiodensity of the example test case phantom, HU analysis was done using Analyze 12.0 toolkit (AnalyzeDirect, Overland Park, United States) by selecting different line profiles within each structure and measuring the HU by calculating the average and the standard deviation over all points related to tho se line profiles. Two different CBCT systems including the Philips Allura FD20 Xper C-arm at 60 kV, 120 mAs, 1 mm^3 voxel size and the ELEKTA XVI linear accelerator (linac) at 120 kV, 264 mAs, 1 mm^3 -voxel size were used in order to observe the density appearance regarding the test prints. For height measurement scale values as a measure of x-ray attenuation of different materials. Therefore, the HU analysis was performed based on the

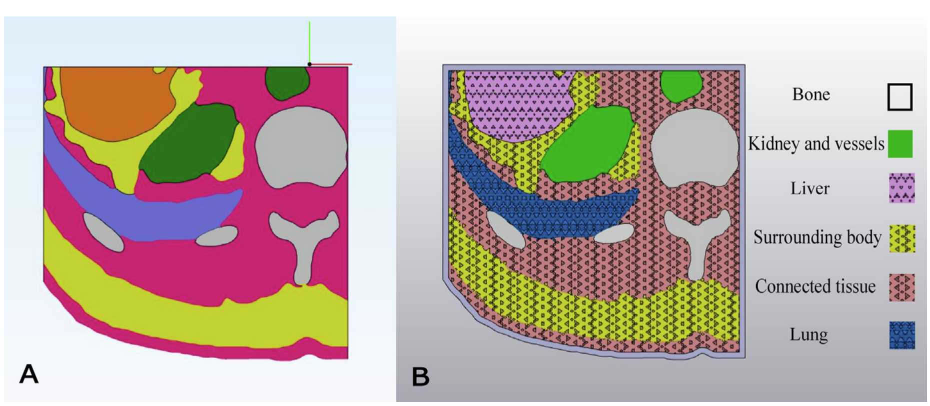

Figure 2. A) represents assembled STL file models imported from 3D Slicer software, B) represents final phantom with the included lattice structures for the corresponding structures in 3Matic software.

Please cite this article as: Hatamikia, S., Oberoi, G., Zacher, A. et al., Additively manufactured test phantoms for mimicking soft tissue radiation attenuation in CBCT using Polyjet technology, Z Med Phys, https://doi.org/10.1016/j.zemedi.2022.05.002

HU values acquired from the standard CT scan of the test phantoms.

2.5 Comparison of HU values from the designed phantom with standard Gammex tissue equivalent phantom

In order to compare the achieved HU values from the developed 3D printed phantom with a standard phantom, we compared the achieved HU values with the Gammex Tissue Characterization Phantom (Gammex Model 467, Middleton, USA). A CT scan from the standard Gammex phantom was acquired with the same CT parameters as for 3D printed test phantoms (Section 2.4).

2.6 Dimensional comparison

2.6.1 Profile comparison using non-contact measurement Profilometer

Fully-automated Profilometer VR-5200 (Keyence, Keyence International, Mechelen, Belgium) with XYZ-axis motorised control was used to validate the dimensions of the 3D printed samples using non-contact measurement technology in 12x magnification and a display resolution of 0.1 µm (Fig. 3 A,B). For height measurement we used Profilometer VR-5200 as it quickly scans an entire surface for reliable measurement of any point on the object. The stage is equipped with a high-precision linear scale and a proprietary sensor, giving a dense data set over an entire area. Based on the light-section method of measurement and automated Profile measurement function, the VR Series automatically calculated the average peak height down to 1 pixel using proprietary light projection patterns. This resulted in highly accurate, ultra-precise measurement. This method was chosen for height measurement of the test samples which included knurled surface (dips and lattice structures) as contact-measurement could give false information.(Fig. 3 C). Multiple measurement data points were applied simultaneously to analyze each data set. Optical Diameter measurement function was used to measure the XY dimension while viewing the target from directly above (Fig. 3 D).

2.6.2 Volumetric comparison using micro-CT

Samples were scanned using micro-CT (Siemens Inveon® µCT, Siemens Medical Solutions, Inc. Molecular Imaging, Knoxville, United States) with the following parameters: 40–50 kV, 200 mA exposure time, one sample per pixel (indicating the number of separate planes in an image), 1024 rows and columns pixel, 9.75µm x 9.75µm spacing, 9.75µm slice thickness. The images were rendered and segmented using Mimics Research 21.0 software

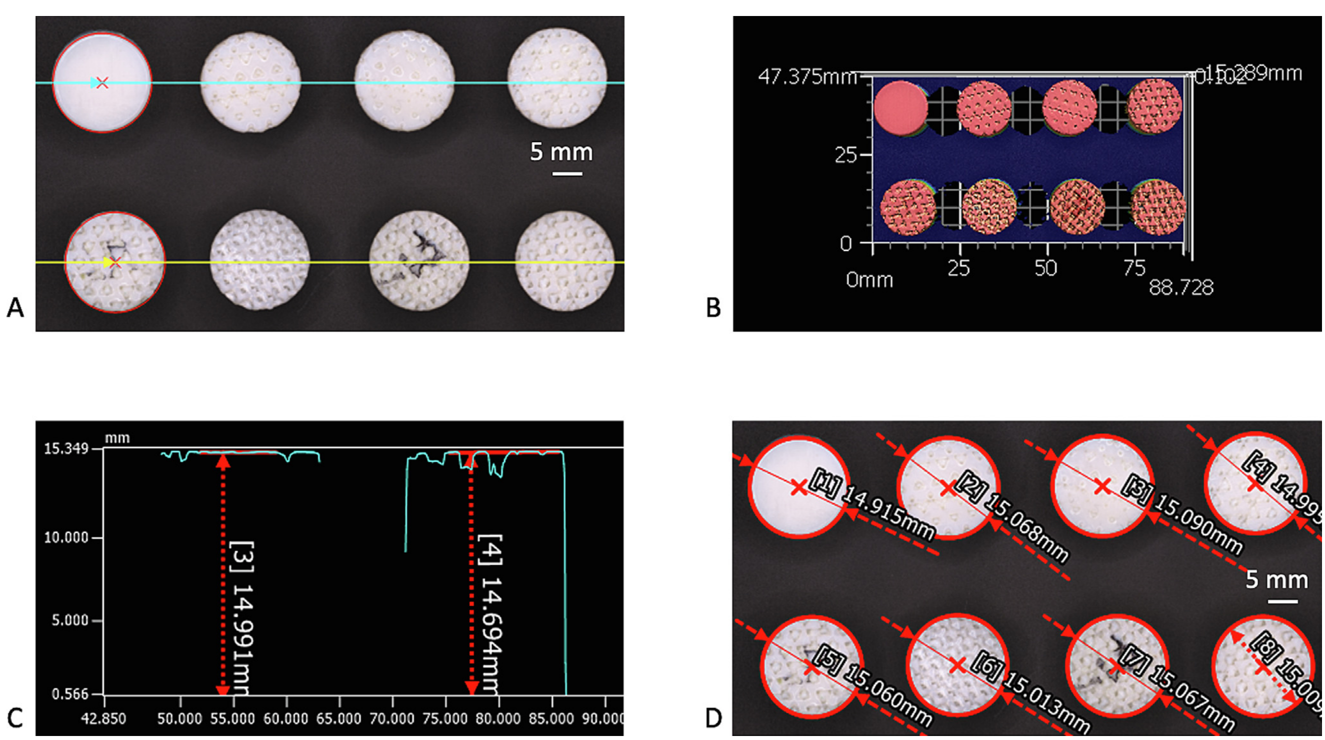

Figure 3. A view of profile comparison using a non-contact measurement profilometer in test phantoms printed in Vero PureWhite. A) Optical profile, B) 3D profile, C) profile graph for test phantom height measurement, D) optical diameter.

(Materialize, Leuven, Belgium). Image-derived volumetric dimensional comparison was performed by comparing the rendered STL files of the micro-CTs of test phantoms over the original STL files (Section 2.1) using Materialize 3-Matic 13.0 software (Materialize, Leuven, Belgium) according to protocol established by our group [13]. The mean difference and standard deviation in the volume of each sample per material, relative to the planned volume in the test phantom design was calculated and graphically plotted. The statistical analysis for dimensional comparison was performed using ANOVA, t-test and Post-hoc Bonferroni correction ($p<0.05$).

3 Results

3.1 Test phantoms design

For the printing process cylindrical structures were derived from the cubic lattice design of test phantoms from R1 to R8 for all the three materials (Fig. 4 A).

3.2 Additively manufactured test phantoms in three different materials and use case phantom

The test phantoms were printed in Vero PureWhite, VeroClear and TangoPlus, with the lattice structure completely replicated from the printed models with a printing resolution of 600 dpi (42.3 μm) in the XY plane and a layer thickness of 30 μm in the Z direction, as verified quantitatively using the profilometer (Fig. 4 B). The printed use case phantom is also shown in Fig. 7 A. In 30 min, we can print 200 cylinders each costing 2 euros per cylinder plus 6 euros printing machine cost. In addition, the material and printing costs related to the use case phantom was 36 euros for a single printout.

3.3 Hounsfield unit analysis for the cylindrical test phantoms

It was possible to create a HU spectrum from a single material using Polyjet technology by means material macrostructure inclusion and regulation of air: material ratio. This is suitable for CBCT phantom design**.** A decreasing gradient in the HU value was seen with an increasing air: material ratio. The axial slices of the resulting CBCT scans from both linac CBCT and C-arm CBCT related to all samples are shown in Fig. 5. The resulting HU values from the three different materials related to all the ratios (R1-R8) is graphically represented in the Fig. 6. The HU range of −757 to +286 was achieved using the test phantoms. Ratio R1 corresponds to the phantom with full printing material (100% material, 0% air). It was possible to replicate the HU of human soft tissues such as fat, muscle, skin, white matter, grey matter, blood, parenchymal organs (e.g., kidney, pancreas, liver) and lungs with every single material [32,33] (Table 1).

3.4 Hounsfield unit analysis for the example use case phantom

According to the HU values achieved in Section 3.3, it was possible to assign the materials and the ratios which corresponded to the organs/tissues density for the use case phantom (Table 2). The axial slice of the resulting scan from linac CBCT related to the example use case phantom is shown in Fig. 7 B. The resulting HU values using the CT scan from this phantom is also reported in the Table 2. According to the results, a good agreement between the target HU values (approximate HU from abdomen CT) and the resulted phantom HU values was achieved at all structures (except for bone) within the phantom. In addition, the resulted HU values in the use case phantom were in a good agreement with the achieved density for the cylindrical test phantoms (Table 1 and Table 2).

3.5 Resulted HU for the Gammex phantom and comparison with the 3D printed phantoms

HU values for different tissue equivalent inserts inside the Gammex phantom including bone mineral, inner bone, liver, brain, solid water, breast, adipose and lung were calculated using the same method for cylindrical test phantoms as described in Section 2.4 (Table 3). The HU values for the other two available inserts inside the Gammex phantom including the cortical bone and CB2 are not reported in this study due to their high HU values. For all three printed test materials, the closest achieved HU to the Gammex phantom inserts and the corresponding ratio (R) is shown in Table 3. According to the results, all the three materials could achieve similar radiodensity range as achieved in the Gammex phantom including 238 HU to −673 HU (bone mineral to lung) when using different ratio values.

3.6 Dimensional comparison

3.6.1 Profilometer

The results from Profilometer (Fig. 8 A, B) showed that the mean height of the test phantoms from R1 to R8 printed in Vero PureWhite, VeroClear and TangoPlus was 14.79 mm, 14.77 mm and 14.58 mm, respectively, and there was no significant difference between the 8 groups of the three materials. The mean diameter of the test phantoms from R1 to R8 printed in Vero PureWhite, VeroClear and TangoPlus was 15.03 mm, 15.10 mm and 14.92 mm, respectively, and there was no significant difference between the 8 groups of the three materials. However, the height and diameter of

Please cite this article as: Hatamikia, S., Oberoi, G., Zacher, A. et al., Additively manufactured test phantoms for mimicking soft tissue radiation attenuation in CBCT using Polyjet technology, Z Med Phys, https://doi.org/10.1016/j.zemedi.2022.05.002

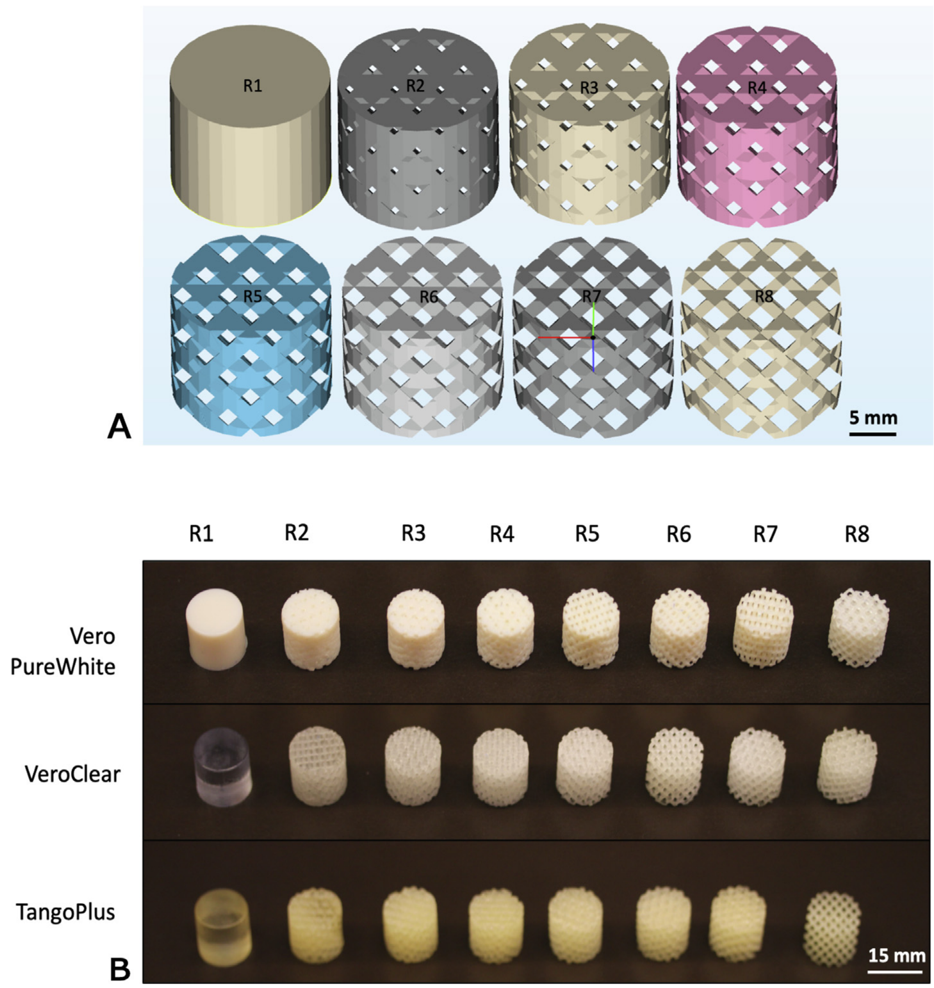

Figure 4. A) Figure showing Stereolithographic (STL) design of the test phantom in eight different R values (ratio of air: material ratios), R1 to R8 in Materialise 3-Matic software, B) Additively manufactured cylindrical test phantoms using three different Polyjet materials from R1 to R8.

the TangoPlus R8 phantoms was slightly lower than the other groups due to the fragility of the material and post-processing damage. The post processing steps (Section 2.3) damaged slightly the fragile flexible TangoPlus lattice structures (mainly R8).

3.6.2 Micro-CT

The results from micro-CT dimensional comparison showed that the samples R7 and R8 in TangoPlus had significantly higher difference in the mean relative volume compared to the designed test phantom volume. The micro-CT images of the test phantoms underwent contrast-based segmentation and automatic volume calculation. TangoPlus being a translucent material with intrinsic lower radiopacity compared to other materials, had lower contrast with air, resulting in partial rendering of the images especially with higher R value (less material), that led to partial volume calculation (Fig. 8 C).

4 Discussion

One main drawback of the Polyjet technology in designing imaging phantoms is the fact that each material leads to a single radiodensity in the printed sample and therefore, distinct radiodensities can only be achieved by developing newer materials. In this study, we developed a strategy to produce imaging phantoms by a modified additive manufacturing technology using a single material in order to reproduce a gradient of HU for human soft tissues (organs to lung) in CBCT by introducing a variable lattice design in the macrostructure without the need of additional fillers. The study is the first demonstration which aims at enabling Polyjet technology to produce a spectrum of radiodensity using a single material. The 3D printed phantoms could produce a HU spectrum equivalent to the radiation attenuation of human soft tissues in the range of −757 to +286 HU on CT. We designed 8 cylindrical test phantoms using 8 dif-

Please cite this article as: Hatamikia, S., Oberoi, G., Zacher, A. et al., Additively manufactured test phantoms for mimicking soft tissue radiation attenuation in CBCT using Polyjet technology, Z Med Phys, https://doi.org/10.1016/j.zemedi.2022.05.002

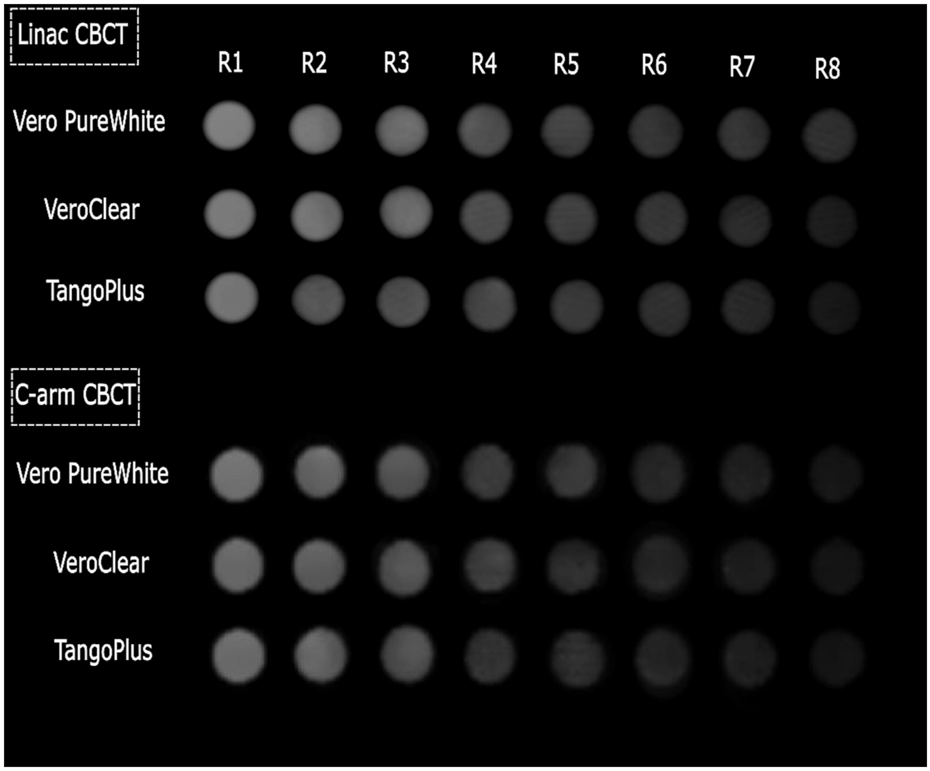

Figure 5. Figure showing the grey value spectrum of the additively manufactured test phantoms derived from CBCT scans. An axial slice of the CBCT using linac CBCT (up) and C-arm CBCT (down) in the three materials Vero PureWhite, VeroClear and TangoPlus using different ratios (R1-R8). The display window shows linear attenuation coefficient and is set to the gray value range [0–4.7].

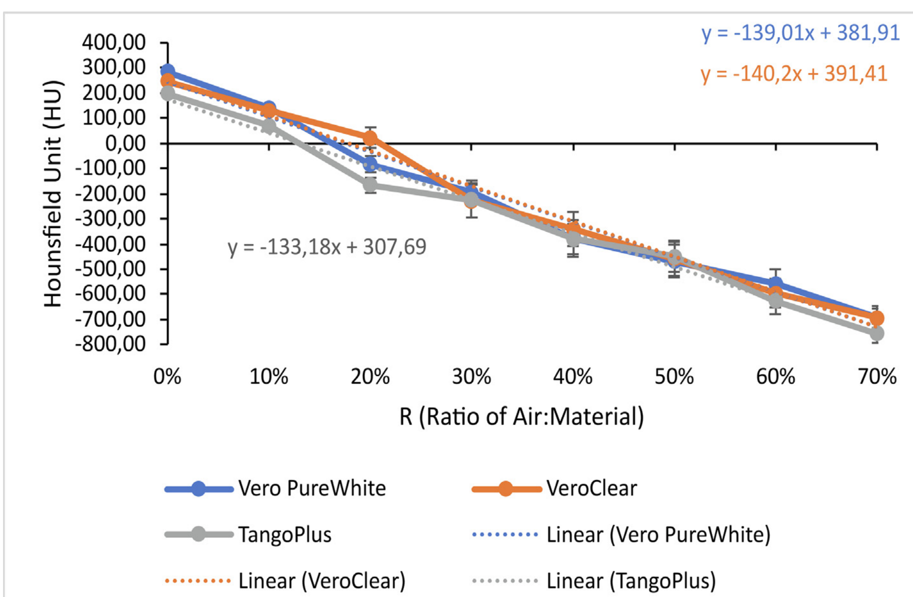

Figure 6. Graph showing the resulting HUs from CT analysis of test phantoms from the three different materials including Vero PureWhite, VeroClear and TangoPlus related to R1 to R8. The linear graphs are a linear approximation of the corresponding graphs.

Please cite this article as: Hatamikia, S., Oberoi, G., Zacher, A. et al., Additively manufactured test phantoms for mimicking soft tissue radiation attenuation in CBCT using Polyjet technology, Z Med Phys, https://doi.org/10.1016/j.zemedi.2022.05.002

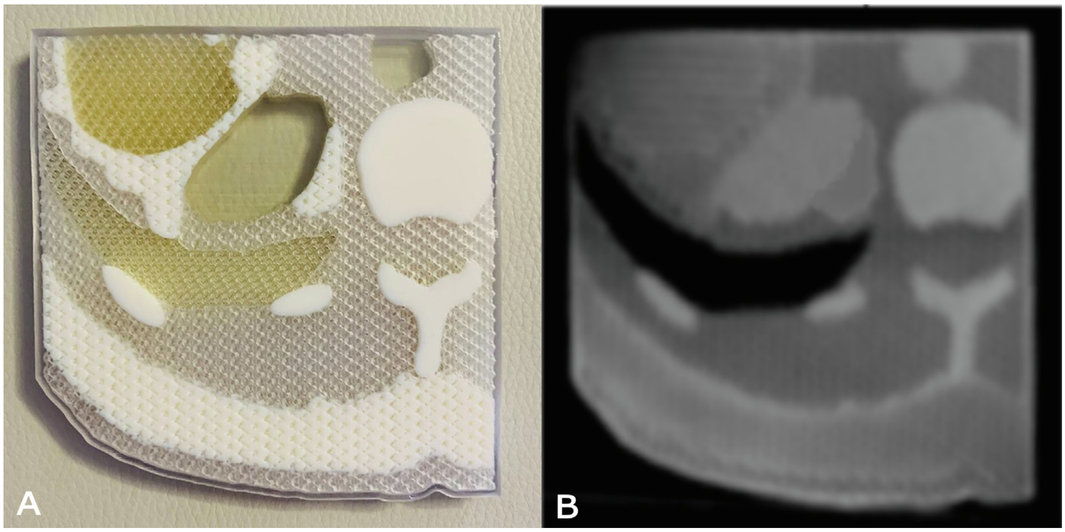

Figure 7. A) Additively manufactured example use case phantom B) An axial slice of the CBCT using linac CBCT. The display window shows linear attenuation coefficient and is set to the gray value range [0–6].

Table 1
Table showing the mean and standard deviation (SD) of the resulting HU of the three different Polyjet materials used in test phantoms, derived from Computed Tomography (CT) analysis and the corresponding soft tissues with equivalence radiodensity.

Ratio R (%)	TangoPlus (HU+SD)	VeroClear (HU+SD)	Vero PureWhite (HU+SD)	Corresponding tissue
R1 (0%)	196.5 ± 11.2	247.5 ± 10.0	286.3 ± 12.1	Organs, Inner bone
R2 (10 %)	69.4 ± 25.1	138.5 ± 15.1	142.9 ± 18.2	Organs, Muscles
R3 (20 %)	−168.2 ± 33.5	29.5 ± 11.7	−86.5 ± 31.3	Fat, Blood, Gray and White matter
R4 (30 %)	−235.9 ± 50.0	−185.1 ± 26.7	−210.3 ± 42.7	Fat, Skin
R5 (40 %)	−381.1 ± 58.6	−318.7 ± 55.1	−366.5 ± 35.4	Fat, Skin
R6 (50 %)	−446.4 ± 40.8	−453.7 ± 21.5	−460.6 ± 44.1	Lung, Skin
R7 (60 %)	−624.3 ± 34.6	−595.7 ± 58.1	−556.6 ± 26.2	Lung, Skin
R8 (70 %)	−757.2 ± 37.8	−694.2 ± 39.3	−698.7 ± 47.1	Lung

ferent air:material ratios with 10% ratio step size. However, smaller ratio step size can be also applied in order to achieve a higher number of different densities using each single material. We also investigated the performance of our approach using a use case phantom including more complex structures and combinations of different lattice structures and materials within the same phantom. Except for bone tissue, a good agreement between the CT HU values and the resulted use case phantom HU values was achieved for all structures. However, we should note that mimicking soft tissue densities was the main aim of this study and the bone tissue density replication was out of scope for this paper. This approach is cost effective and improves the sustainability of Polyjet technology and the available materials. By changing the air:material ratio of the lattice design digitally, a spectrum of grey value can be added to the available materials' intrinsic radiation attenuation. Depending on the selected step size for ratio value (R), similar HU values to Gammex phantom were achieved for some 3D printed materials, e.g., in case of liver insert, 3D printed phantom using TangoPlus (R2) (69 HU) showed a very similar HU to the liver inserted Gammex (66 HU) while for some other materials some differences can be seen e.g., VeroPureWhite (R2) (142 HU). The reason is evident; the step size of the ratio (R) selected was rather large (10%) and smaller step size is required in order to reach specific HU values for each material. However, as all the three employed materials could cover the full range as achieved in the standard Gammex phantom inserts (except for cortical bone and CB2) including 238 HU to −673 (bone mineral to lung), achieving target HU for each material is fully feasible using additional ratio values (R) when reducing the ratio step size.

Test phantoms printed with this approach displayed geometrical accuracy assigned to the digital models, as seen in the dimensional analysis with micro-CT and non-contact profile measurement. The non-contact measurement was a

Table 2
Table showing the mean and standard deviation (SD) of the resulting HU of the example test case phantom compared to target HU values (approximate HU from abdomen CT) as well as corresponding cylindrical test phantoms derived from CT analysis.

Target tissue	Approximate HU values related to the target tissues	Selected material and ratio	HU values related to the selected materials	HU values resulted from the example test case phantom
Bone	759.2 ± 54.1	Vero PureWhite (R1)	286.3 ± 12.1	245.2 ± 36.9
Kidney and vessels	175.3 ± 34.3	TangoPlus (R1)	196.5 ± 11.2	165.4 ± 23.2
Liver	96.1 ± 30.5	TangoPlus (R2)	69.4 ± 25.1	85.7 ± 18.7
Surrounding body	32.8 ± 27.5	VeroClear (R3)	29.5 ± 11.7	23.8 ± 12.4
Connected tissue	−65.7 ± 38.4	Vero PureWhite (R3)	−86.5 ± 31.3	−100.3 ± 20.7
Lung	−794.5 ± 29.8	TangoPlus (R8)	−757.2 ± 37.8	−778.6 ± 33.6

Table 3
Table showing the mean and standard deviation (SD) of the resulting HU related to the Gammex tissue equivalent inserted cylinders including bone mineral, inner bone, liver, brain, solid water, breast, adipose and lung and the corresponding materials with different ratios used in the printed test phantoms.

Gammex phantom	CT value (HU+SD)	Designed phantom	CT value (HU+SD)
Bone mineral	238 ± 17	TangoPlus (R1), VeroClear (R1) VeroPureWhite (R1)	196.5 ± 11.1 247.5 ± 10.0 286.3 ± 12.1
Inner bone	210 ± 12	TangoPlus (R1), VeroClear (R1) VeroPureWhite (R2)	196.5 ± 11.1, 247.5 ± 10.0 142.9 ± 18.2
Liver	66 ± 10	TangoPlus (R2), VeroClear (R3) VeroPureWhite (R2)	69.4 ± 25.1, 29.5 ± 11.7 142.9 ± 18.2
Brain	24 ± 6	TangoPlus (R2), VeroClear (R3) VeroPureWhite (R3)	69.4 ± 25.1, 29.5 ± 11.7 −86.5 ± 31.3
Solid Water	−1 ± 3	TangoPlus (R2), VeroClear (R3) VeroPureWhite (R3)	69.4 ± 25.1, 29.5 ± 11.7 −86.5 ± 31.3
Breast	−72 ± 10	TangoPlus (R3), VeroClear (R3) VeroPureWhite (R3)	−168.2 ± 33.5, 29.5 ± 11.7 −86.5 ± 31.3
Adipose	−109 ± 13	TangoPlus (R3), VeroClear (R4) VeroPureWhite (R3)	−168.2 ± 33.5, −185.1 ± 26.7 −86.5 ± 31.3
Lung-450	−475 ± 12	TangoPlus (R6), VeroClear (R6) VeroPureWhite (R6)	−446.4 ± 40.8, −453.7 ± 21.5 −460.6 ± 44.1
Lung-300	−673 ± 15	TangoPlus (R7), VeroClear (R8) VeroPureWhite (R8)	624.3 ± 34.6, −694.2 ± 39.4 −698.8 ± 47.1

very useful feature in this study for flexible TangoPlus phantoms in combinaton with micro-CT. Profiles from different angles can be combined, allowing for measurement as a single piece of data. Overall, the proposed strategy establishes a non-sophisticated, customized design for building cost-effective imaging phantoms with commonly available 3D printing materials.

Several attempts at building imaging test phantoms have been made with FDM, SLA and Polyjet printing using ABS and acrylonitrile-styrene-acrylate (ASA) from FDM, Viso-Clear from SLA materials, VeroClear and Tango from PolyJet [29]. Strategies using FDM technology have been described to obtain a range of radiodensities for CT by changing the infill density [34–36]. PLA/ Calcium filament blends have previously been used with FDM to produce test cubes with radiodensity up to 518 HU, reproducing bone attenuation [37]. In another study, PLA and StoneFil PLA-concrete were used to print a phantom at several in-fill densities, to achieve quasi-simultaneous 3D printing of muscle-, lung- and bone-equivalent media [24]. However, FDM is limited by large nozzle size and rigging mechanism. Developments include SLA system for printing an anthropomorphic thorax phantom using standard clear photocurable resin (Clear Resin V04, Formlabs Inc.) for image optimization in digital X-ray imaging [38]. The radiation dose on diagnostic image quality was assessed for standardization of imaging parameters and appearance. The necessity to de-noise the clinical image and missing of fine structures

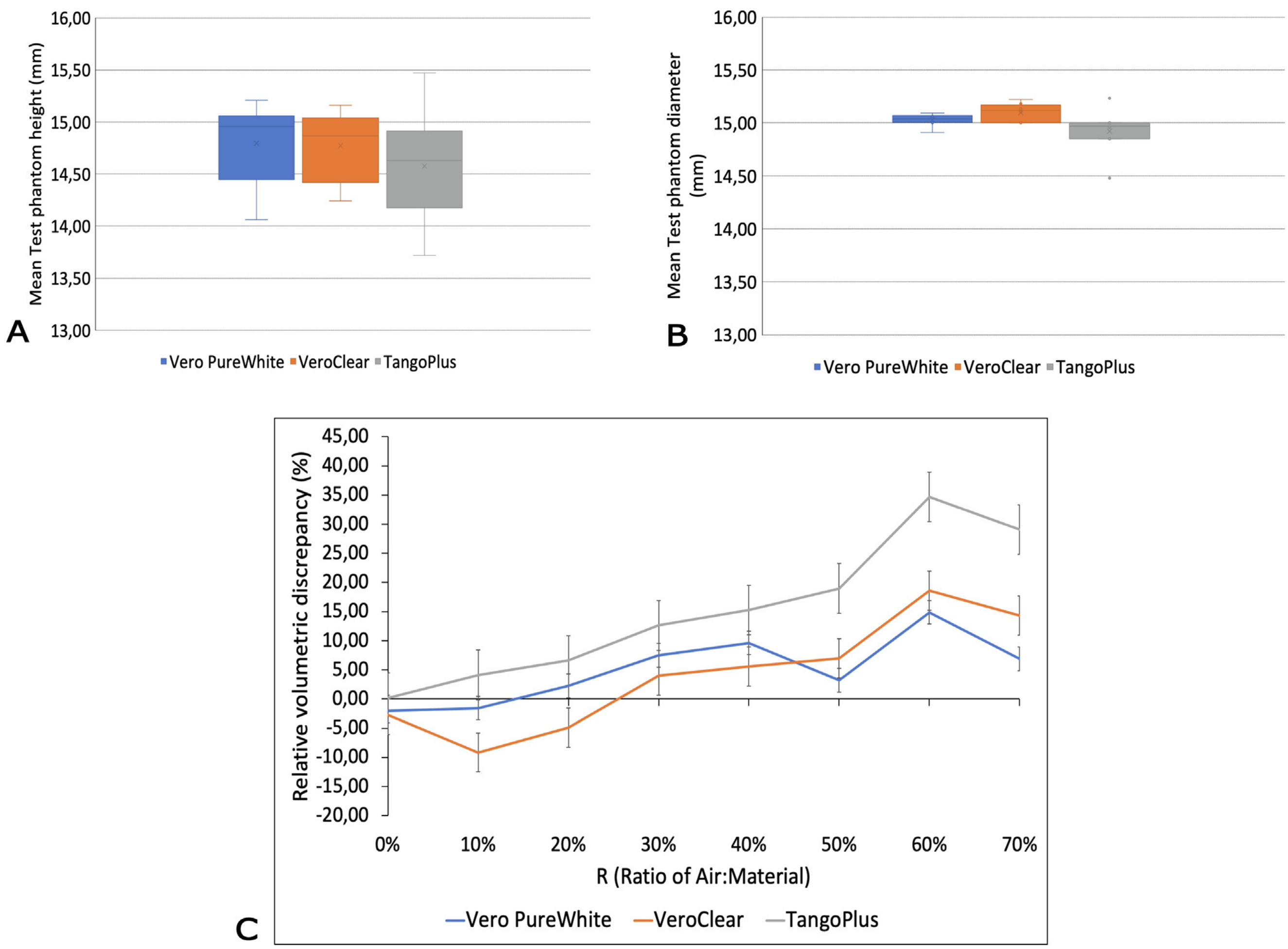

Figure 8. Figure showing the results from dimensional comparisons. A) Graph showing the results from non-contact profilometer measurement A) mean height, and B) mean diameter, for additively manufactured test phantoms in three different materials in ratios R1 to R8, C) Results from micro-CT volumetric comparison for test phantoms printed in three different materials from R1 to R8.

in the printed phantom led to lack of detail in the achieved image quality. Nonetheless, SLA does not allow multimaterial prints. To overcome these technological limitations, we proposed a modified Polyjet printing technology, using a simple algorithm as mentioned in section 2.1 adding an asset to a material's intrinsic radiological properties. In contrast to previous studies using micro-CT for dimensional analysis with contrast-dependent issues, non-contact measurement system Profilometer additionally was used in this study conventional contact-based systems can easily miss small surface changes [12,13].

This study employs Polyjet technology due to its higher resolution (16–32 µm), accuracy (±0.05 mm) and flexibility in assigning and reproducing macrostructures in the printed model [39]. The realization of test phantom was based on two factors, printing efficiency (in terms of resolution) and the post-printing cleaning process. During experiments it was seen that it is possible to print a lattice structure with minimum material thickness in the range of 0.03 mm, but this is hard to clean, especially flexible TangoPlus material. So, the minimum material dimension for a lattice (independent of shape and design) was chosen as 0.4 mm with 10% increment in the material volume per cube. This algorithm and R value (air:material ratio) can be applied to any shape such as spheres, cubes, pyramids, to achieve the desired radiodensity spectrum. In addition, Polyjet technology offers another advantage over other printing technologies by offering a bigger (490 x 390 x 200 mm) built platform [40–42]. In the previous studies using Polyjet printing materials to build imaging phantoms, single material represented a specific radiation attenuation in a single printing cycle [12,18,43,44]. This study is the first demonstration which proposes a methodology to enable Polyjet technology in order to create different HUs within one material, increasing the sustainability of the existing materials and technology. We proposed to

Please cite this article as: Hatamikia, S., Oberoi, G., Zacher, A. et al., Additively manufactured test phantoms for mimicking soft tissue radiation attenuation in CBCT using Polyjet technology, Z Med Phys, https://doi.org/10.1016/j.zemedi.2022.05.002

use this technique for CBCT and verified it with three materials and two CBCT systems.

In a recent study [4], the authors propose a PixelPrint approach using 3D printing technique in order to create a patient-based lung phantom with accurate textures and attenuation profiles. They used a filament printing technique which controlled the filament ratio and could continuously modify the printing speed. In another recent study [45], we used filament printing technique in order to develop a CT-derived 3D printed thorax phantom which can mimic realistic bone- and soft-equivalent radiodensity by means of commercially available filaments. The fabricated 3D printed thorax phantom could closely resemble the geometry of patient and could create life-like heterogeneity within the printed structures. Although these studies presented heterogeneity within the printed model and could mimic realistic radiodensity, the large nozzle size restricts the printing resolution at macrostructure level. In contrast, the proposed PolyJet technique introduced in this study enables simultaneous multi-material printing of a model with a very high resolution in the range of 32 micrometer. In another study using Polyjet technology [12], we developed a CT-based modified 3D printing technique in order to print a hollow thorax phantom which could replicate skeletal morphology of the patient. However, an indirect printing process was used and the printed hollow phantom needed to be filled by a radiopaque amalgamate at different combinations in order to reproduce a spectrum of radiodensity as in human thorax. The current study enhanced this study [12] and also other previous studies using Polyjet technology [18] by enabling the Polyjet technology to mimic a spectrum of radiodensity using a single material.

In this study, HU values were calculated based on a standard CT scan from the phantoms due to the inability of CBCT to show the actual HU [30, 31]. We observed that at higher resolution than 1 mm^3 the lattice structure becomes visible in CBCT scan of test phantoms for some ratios (especially at R8 and R7). For conventional CT, the usefulness of this technology depends on the application. While the fine structure of the material is barely visible in CBCT with 1 mm^3 resolution due to various artifacts and increased scatter radiation [6] associated with this imaging modality, the lattice-type fine structure of the phantom material becomes visible in conventional CT. However, nowadays, the CBCT imaging with up to 1 mm^3 resolution is the standard for many clinical scenarios and its applications are quite large and developing phantoms in this area is of great importance. Although commercially available CBCT phantoms have been designed and validated for medical imaging approaches, our proposed methodology provides the opportunity to different research groups to design their own case-specific CBCT phantoms for validation of the new developed imaging algorithms and assists verification of variety of research purposes using the accurate, high resolution, commonly available, Polyjet printing technology. The proposed phantom design in this study includes a cost-effective protocol compared to available commercial phantoms as well as our previous approaches [12]. We should note that using our proposed protocol, the costs of material and printing time are less compared to the personal costs of the manual cleaning, which can be calculated with 2 person hours per model.

This research was a proof-of-concept study in which the construction, radiation attenuation and geometrical accuracy of the additive manufacturing-guided imaging phantom fabrication was validated. Hence, the forthcoming research will be implementing a defined approach on a customized imaging phantom. Further material modification and biomimetic lattice designs could be examined to investigate the possible extension of the achieved HU range.

Declaration of Competing Interest

The authors declare that they have no known competing financial interests or personal relationships that could have appeared to influence the work reported in this paper.

Acknowledgment

This study has received funding from the Austrian Center for Medical Innovation and Technology (ACMIT), within the scope of the COMET program, Austrian BMVIT, BMWFW and the governments of Lower Austria and Tyrol. The additive manufacturing infrastructure used in this study has received funding by the Austrian Research Promoting Agency (FFG) within the M3dRES project (Grant No. 858060).

References

[1] Jaffray DA, Siewerdsen JH. Cone-beam computed tomography with a flat-panel imager: initial performance characterization. Med Phys 2000;27:1311–1323. https://doi.org/10.1118/1.599009.

[2] Czerny C, Eichler K, Croissant Y, Schulz B, Kronreif G, Schmidt R, et al. Combining C-arm CT with a new remote operated positioning and guidance system for guidance of minimally invasive spine interventions. J Neurointerv Surg 2015;7:303–308. https://doi.org/10.1136/neurintsurg-2013-011034.

[3] Orth RC, Wallace MJ, Kuo MD. Technology Assessment Committee of the Society of Interventional Radiology. C-arm cone-beam CT: general principles and technical considerations for use in interventional radiology. J Vasc Interv Radiol 2008;19:814–820. https://doi.org/10.1016/j.jvir.2008.02.002.

[4] Mei K, Geagan M, Roshkovan L, Litt HI, Gang GJ, Shapira N, et al. Three-dimensional printing of patient-specific lung phantoms for CT imaging: Emulating lung tissue with accurate attenuation profiles and textures. Med Phys 2022;49:825–835. https://doi.org/10.1002/mp.15407.

[5] Zbijewski W, De Jean P, Prakash P, Ding Y, Stayman JW, Packard N, et al. A dedicated cone-beam CT system for musculoskeletal extremities imaging: design, optimization, and initial performance characterization. Med Phys 2011;38:4700–4713. https://doi.org/10.1118/1.3611039.

[6] Hatamikia S, Biguri A, Kronreif G, Kettenbach J, Russ T, Furtado H, et al. Optimization for customized trajectories in cone beam computed tomography. Med Phys 2020;47:4786–4799. https://doi.org/10.1002/mp.14403.

[7] Gang GJ, Zbijewski W, Mahesh M, Thawait G, Packard N, Yorkston J, et al. Image quality and dose for a multisource cone-beam CT extremity scanner. Med Phys 2018;45:144–155. https://doi.org/10.1002/mp.12659.

[8] Carrino JA, Al Muhit A, Zbijewski W, Thawait GK, Stayman JW, Packard N, et al. Dedicated cone-beam CT system for extremity imaging. Radiology 2014;270:816–824. https://doi.org/10.1148/radiol.13130225.

[9] Weiss R, Read-Fuller A. Cone Beam Computed Tomography in Oral and Maxillofacial Surgery. An Evidence-Based Review. Dentistry J 2019;7. https://doi.org/10.3390/dj7020052.

[10] Wang H, Nie K, Chang J, Kuang Y. A Monte Carlo study to investigate the feasibility of an on-board SPECT/spectral-CT/CBCT imager for medical linear accelerator. Med Phys 2020;47:5112–5122. https://doi.org/10.1002/mp.14398.

[11] Roberts PR, Jani AB, Packianathan S, Albert A, Bhandari R, Vijayakumar S. Upcoming imaging concepts and their impact on treatment planning and treatment response in radiation oncology. Radiat Oncol 2018;13:146. https://doi.org/10.1186/s13014-018-1091-1.

[12] Hatamikia S, Oberoi G, Unger E, Kronreif G, Kettenbach J, Buschmann M, et al. Additively Manufactured Patient-Specific Anthropomorphic Thorax Phantom With Realistic Radiation Attenuation Properties. Front Bioeng Biotechnol 2020;8:385. https://doi.org/10.3389/fbioe.2020.00385.

[13] Oberoi G, Eberspächer-Schweda MC, Hatamikia S, Königshofer M, Baumgartner D, Kramer A-M, et al. 3D printed biomimetic rabbit airway simulation model for nasotracheal intubation training. Front Vet Sci 2020;7:. https://doi.org/10.3389/fvets.2020.587524587524.

[14] Al-Halabi H, Portelance L, Duclos M, Reniers B, Bahoric B, Souhami L. Cone beam CT-based three-dimensional planning in high-dose-rate brachytherapy for cervical cancer. Int J Radiat Oncol Biol Phys 2010;77:1092–1097. https://doi.org/10.1016/j.ijrobp.2009.06.036.

[15] Tino R, Leary M, Yeo A, Kyriakou E, Kron T, Brandt M. Additive manufacturing in radiation oncology: a review of clinical practice, emerging trends and research opportunities. Int J Extrem Manuf 2020;2:. https://doi.org/10.1088/2631-7990/ab70af012003.

[16] Cloonan AJ, Shahmirzadi D, Li RX, Doyle BJ, Konofagou EE, McGloughlin TM. 3D-Printed Tissue-Mimicking Phantoms for Medical Imaging and Computational Validation Applications. 3D Print Addit Manuf 2014;1:14–23. https://doi.org/10.1089/3dp.2013.0010.

[17] Alssabbagh M, Tajuddin AA, Abdulmanap M, Zainon R. Evaluation of 3D printing materials for fabrication of a novel multi-functional 3D thyroid phantom for medical dosimetry and image quality. Radiat Phys Chem 2017;135:106–112. https://doi.org/10.1016/j.radphyschem.2017.02.009.

[18] Kim M-J, Lee S-R, Lee M-Y, Sohn JW, Yun HG, Choi JY, et al. Characterization of 3D printing techniques: Toward patient specific quality assurance spine-shaped phantom for stereotactic body radiation therapy. PLoS One 2017;12:. https://doi.org/10.1371/journal.pone.0176227e0176227.

[19] Zhang F, Zhang H, Zhao H, He Z, Shi L, He Y, et al. Design and fabrication of a personalized anthropomorphic phantom using 3D printing and tissue equivalent materials. Quant Imaging Med Surg 2019;9:94–100. https://doi.org/10.21037/qims.2018.08.01.

[20] Filippou V, Tsoumpas C. Recent advances on the development of phantoms using 3D printing for imaging with CT, MRI, PET, SPECT, and ultrasound. Med Phys 2018. https://doi.org/10.1002/mp.13058.

[21] Dancewicz OL, Sylvander SR, Markwell TS, Crowe SB, Trapp JV. Radiological properties of 3D printed materials in kilovoltage and megavoltage photon beams. Phys Med 2017;38:111–118. https://doi.org/10.1016/j.ejmp.2017.05.051.

[22] Ceh J, Youd T, Mastrovich Z, Peterson C, Khan S, Sasser TA, et al. Bismuth infusion of ABS enables additive manufacturing of complex radiological phantoms and shielding equipment. Sensors (Basel) 2017;17. https://doi.org/10.3390/s17030459.

[23] Savi M, Andrade MAB, Potiens MPA. Commercial filament testing for use in 3D printed phantoms. Radiat Phys Chem 2020;174:. https://doi.org/10.1016/j.radphyschem.2020.108906108906.

[24] Kairn T, Zahrani M, Cassim N, Livingstone AG, Charles PH, Crowe SB. Quasi-simultaneous 3D printing of muscle-, lung- and bone-equivalent media: a proof-of-concept study. Phys Eng Sci Med 2020;43:701–710. https://doi.org/10.1007/s13246-020-00864-5.

[25] Mayer R, Liacouras P, Thomas A, Kang M, Lin L, Simone CB. 3D printer generated thorax phantom with mobile tumor for radiation dosimetry. Rev Sci Instrum 2015;86:. https://doi.org/10.1063/1.4923294074301.

[26] Maier J, Weiherer M, Huber M, Palm C. Imitating human soft tissue on basis of a dual-material 3D print using a support-filled metamaterial to provide bimanual haptic for a hand surgery training system. Quant Imaging Med Surg 2019;9:30–42. https://doi.org/10.21037/qims.2018.09.17.

[27] Kwon J, Ock J, Kim N. Mimicking the Mechanical Properties of Aortic Tissue with Pattern-Embedded 3D Printing for a Realistic Phantom. Materials (Basel) 2020;13. https://doi.org/10.3390/ma13215042.

[28] Kim T, Kim GB, Song HK, Kyung YS, Kim C-S, Kim N. Accuracies of 3D printers with hard and soft materials. Rapid Prototyp J 2020. https://doi.org/10.1108/RPJ-09-2019-0236.

[29] Silvestro E, Betts KN, Francavilla ML, Andronikou S, Sze RW. Imaging properties of additive manufactured (3D printed) materials for potential use for phantom models. J Digit Imaging 2020;33:456–464. https://doi.org/10.1007/s10278-019-00257-5.

[30] Pauwels R, Jacobs R, Singer SR, Mupparapu M. CBCT-based bone quality assessment: are Hounsfield units applicable? Dentomaxillofac Radiol 2015;44:20140238. https://doi.org/10.1259/dmfr.20140238.

[31] Thing RS, Bernchou U, Mainegra-Hing E, Hansen O, Brink C. Hounsfield unit recovery in clinical cone beam CT images of the thorax acquired for image guided radiation therapy. Phys Med Biol 2016;61:5781–5802. https://doi.org/10.1088/0031-9155/61/15/5781.

[32] Patrick S, Birur NP, Gurushanth K, Raghavan AS, Gurudath S. Comparison of gray values of cone-beam computed tomography with hounsfield units of multislice computed tomography: An in vitro study. Indian J Dent Res 2017;28:66–70. https://doi.org/10.4103/ijdr.IJDR_415_16.

[33] Chougule VN, Mulay A, Ahuja BB. Clinical Case Study: Spine Modeling for Minimum Invasive Spine Surgeries (MISS) using Rapid Prototyping; 2017.

[34] Madamesila J, McGeachy P, Villarreal Barajas JE, Khan R. Characterizing 3D printing in the fabrication of variable density phantoms for quality assurance of radiotherapy. Phys Med 2016;32:242–247. https://doi.org/10.1016/j.ejmp.2015.09.013.

Please cite this article as: Hatamikia, S., Oberoi, G., Zacher, A. et al., Additively manufactured test phantoms for mimicking soft tissue radiation attenuation in CBCT using Polyjet technology, Z Med Phys, https://doi.org/10.1016/j.zemedi.2022.05.002

[35] García-Domínguez A, Claver J, Camacho AM, Sebastián MA. Considerations on the applicability of test methods for mechanical characterization of materials manufactured by FDM. Materials (Basel) 2019;13. https://doi.org/10.3390/ma13010028.

[36] Podroužek J, Marcon M, Nin evi K, Wan-Wendner R. Bio-Inspired 3D Infill Patterns for Additive Manufacturing and Structural Applications. Materials (Basel) 2019;12. https://doi.org/10.3390/ma12030499.

[37] Popescu AT, Stan O, Miclea L. 3D printing bone models extracted from medical imaging data. 2014 IEEE International Conference on Automation, Quality and Testing, Robotics, IEEE; 2014, p. 1–5. doi:10.1109/AQTR.2014.6857890.

[38] Irnstorfer N, Unger E, Hojreh A, Homolka P. An anthropomorphic phantom representing a prematurely born neonate for digital x-ray imaging using 3D printing: Proof of concept and comparison of image quality from different systems. Sci Rep 2019;9:14357. https://doi.org/10.1038/s41598-019-50925-3.

[39] Kluska E, Gruda P, Majca-Nowak N. The accuracy and the printing resolution comparison of different 3D printing technologies. Trans Aerosp Res 2018;2018:69–86. https://doi.org/10.2478/tar-2018-0023.

[40] FDM vs. PolyJet | 3D Printing Technology Comparison | Stratasys Direct n.d. https://www.stratasysdirect.com/manufacturing-services/3d-printing/fdm-vs-polyjet-tale-of-two-3d-printing-technologies (accessed October 4, 2021).

[41] Kristiawan RB, Imaduddin F, Ariawan D, Ubaidillah AZ. A review on the fused deposition modeling (FDM) 3D printing: Filament processing, materials, and printing parameters. Open Eng 2021;11:639–649. https://doi.org/10.1515/eng-2021-0063.

[42] Mwema FM, Akinlabi ET. Basics of fused deposition modelling (FDM). Fused deposition modeling: strategies for quality enhancement. Cham: Springer International Publishing; 2020. p. 1–15.

[43] Ibrahim D, Broilo TL, Heitz C, de Oliveira MG, de Oliveira HW, Nobre SMW, et al. Dimensional error of selective laser sintering, three-dimensional printing and PolyJet models in the reproduction of mandibular anatomy. J Craniomaxillofac Surg 2009;37:167–173. https://doi.org/10.1016/j.jcms.2008.10.008.

[44] Ionita CN, Mokin M, Varble N, Bednarek DR, Xiang J, Snyder KV, et al. Challenges and limitations of patient-specific vascular phantom fabrication using 3D Polyjet printing. Proc SPIE 2014;9038:90380M. https://doi.org/10.1117/12.2042266.

[45] Hatamikia S, Kronreif G, Unger A, Oberoi G, Jaksa L, Unger E, et al. 3D printed patient-specific thorax phantom with realistic heterogenous bone radiopacity using filament printer technology. Z Med Phys 2022. https://doi.org/10.1016/j.zemedi.2022.02.001.

Please cite this article as: Hatamikia, S., Oberoi, G., Zacher, A. et al., Additively manufactured test phantoms for mimicking soft tissue radiation attenuation in CBCT using Polyjet technology, Z Med Phys, https://doi.org/10.1016/j.zemedi.2022.05.002